Scientific Reports

https://doi.org/10.1038/s41598-025-34508-z

Article in Press

Numerical simulation of hydraulic–natural fracture interaction based on the continuous–discontinuous element method

Received: 17 August 2025

Accepted: 29 December 2025

Published online: 05 January 2026

Cite this article as: Yang K., Huang G., Zhou F. *et al.* Numerical simulation of hydraulic–natural fracture interaction based on the continuous–discontinuous element method. *Sci Rep* (2025). https://doi.org/10.1038/s41598-025-34508-z

Kai Yang, Guopeng Huang, Fujian Zhou, Tianbo Liang, Jie Zuo & Minghui Li

Numerical simulation of hydraulic–natural fracture interaction based on the continuous–discontinuous element method

Kai Yang[1,2], Guopeng Huang[1,2], Fujian Zhou[1,2]*, Tianbo Liang[1,2], Jie Zuo[1,2], Minghui Li[3,4]

1 State Key Laboratory of Petroleum Resources and Engineering, China University of Petroleum (Beijing), Beijing 102249, China

2 Unconventional Petroleum Research Institute, China University of Petroleum (Beijing), Beijing, 102249, China

3 Research Institute of Petroleum Exploration & Development, PetroChina Corporation, Beijing 100083, China

4 Oil & Gas and New Energy Branch, PetroChina Corporation, Beijing 100010, China

*Corresponding Author: Fujian Zhou (zhoufj@cup.edu.cn)

Abstract: Shale reservoirs commonly contain numerous geological discontinuities, such as natural fractures, faults, and lithological interfaces. These discontinuities significantly influence the formation of hydraulic fracture networks. Therefore, to investigate the impact of different natural fracture parameters on fracture network development, this study establishes a stress-seepage-fracture multi-field coupling model for fractured reservoirs based on the continuous-discontinuous algorithm. The effects of natural fracture angle, stress difference, natural fracture strength, and injection rate on fracture network morphology, injection pressure, and fracture complexity are systematically analyzed. The results indicate that the natural fracture angle and stress difference jointly control fracture propagation patterns. At high natural fracture angles and high stress differences, hydraulic fractures tend to directly cross natural fractures. Additionally, as natural fracture strength increases, the difficulty of natural fracture activation gradually rises, while the number of branch fractures increases. Under high injection rates, the fluid pressure builds up rapidly, facilitating better activation of natural fractures. Meanwhile, as the injection rate increases, the growth rate of fracture complexity accelerates significantly. However, under the same injected volume, the fracture complexity is highest at 0.001 m^3/s and lowest at 0.01 m^3/s. This study aims to provide guidance for understanding the interaction mechanisms between hydraulic and natural fractures and optimizing fracturing design parameters.

Keywords: Continuous-discontinuous element method; Natural fracture; Fracture

network；Hydraulic fracturing

1 Introduction

Unconventional oil and gas resources have become a crucial component of the global oil and gas supply[1–4]. Hydraulic fracturing technology is the key technical means for the economic development of unconventional reservoirs[5]. Unconventional reservoirs typically exhibit low porosity, low permeability, and strong heterogeneity, with widespread geological discontinuities such as natural fractures and weak planes[6,7]. These geological discontinuities significantly influence the propagation path of hydraulic fractures, thereby further affecting hydrocarbon production. Therefore, in-depth investigation of the interaction mechanisms between hydraulic fractures and natural fractures is essential for optimizing fracturing parameters and enhancing well productivity. Weng et al.[8] classified the interaction modes between hydraulic fractures (HFs) and natural fractures (NFs) into five categories: (i) direct penetration of the HF through the NF, (ii) crossing with or without offset, (iii) intersection between fracture trajectories, (iv) branching, and (v) shear slip along the NF. Zheng et al.[9] evaluated parameters such as the approach angle, fluid viscosity, and injection rate, and developed qualitative diagrams to illustrate their respective influences on HF propagation. Bakhshi et al.[10] demonstrated how different orthotropic in-situ stress states, friction angles, tensile strengths, and shear strengths of natural fractures affect the interaction behavior of cemented and uncemented fractures at various approach angles, and constructed diagrams depicting arresting, opening, and crossing scenarios.

In recent decades, numerous scholars have investigated hydraulic fracture propagation behavior through theoretical analysis, numerical simulation, and laboratory experiments[11,12]. For theoretical models, the primary approaches include the KGD model[13], PKN model[14], and Penny-shaped model[15]. However, these theoretical models are often based on numerous assumptions and fail to account for the influence of interactions between hydraulic fractures and natural fractures[16]. Various numerical algorithms have been developed to enable further investigation of interaction mechanisms between hydraulic fractures and natural fractures under complex scenarios, including finite element method (FEM[17,18]), discrete element method (DEM[19–21]), boundary element method (BEM[22,23]), and extended finite element method (XFEM)[24,25]. The DEM discretizes the rock matrix into individual rigid blocks interconnected through contacts. The explicit difference method is employed to simulate the mutual motion and interaction between these rigid blocks. The discontinuous interfaces formed between the rigid blocks can effectively characterize fractures and rock defects. Chong[26], Fatahi[27], Lyu et al[28]. have utilized DEM to investigate the interaction mechanisms between hydraulic fractures and natural fractures. The BEM discretizes only the domain boundaries or discontinuous interfaces, significantly reducing model complexity. Olson et al. first employed two-dimensional displacement discontinuity method (DDM) to simulate hydraulic fracture propagation. Zheng et al.[29] utilized a boundary element method incorporating rock failure criteria to demonstrate the influence of hydraulic fracture geometry on fracture interaction mechanisms. The extended finite element method (XFEM) achieves mesh-independent fracture propagation simulation by incorporating enriched discontinuous shape functions into conventional finite element displacement interpolation functions, thereby representing displacement field discontinuities without requiring mesh refinement[30]. In recent years, hybrid algorithms combining the advantages of different numerical methods have been proposed for enhanced fracture simulation. Zhang et al.[31] proposed a novel XFEM-PFM coupled approach for hydraulic fracturing simulation and investigated the interaction mechanisms between hydraulic fractures and natural fractures. Zhu et al.[32] developed a hybrid FEM-DEM numerical algorithm that combines the advantages of both finite element and discrete element methods to simulate hydraulic fracture propagation.

Hybrid methods demonstrate superior advantages in hydraulic fracture propagation simulation, yet their application in complex scenarios requires further investigation. In this study, a stress-seepage-fracture multi-field coupling algorithm based on the continuous-discontinuous method was developed to investigate the interaction behavior between hydraulic fractures and natural fractures in fractured reservoirs. The interaction behavior was validated against theoretical criteria. Furthermore, the coupled effects of natural fracture angles and stress differences, natural fracture strength, and injection rate on fracture geometry, pressure response, and stimulation effectiveness were systematically analyzed. The paper is organized as follows: Section 2 introduces the numerical methodology and coupling scheme; Section 3 describes the model construction and simulation schemes; Sections 4 and 5 present the interaction results for a single natural fracture and natural fracture networks, respectively; and Section 6 summarizes the main findings, significance, limitations, and future research directions.

2 Numerical methods

The continuum-discontinuum algorithm integrates the advantages of the finite element method and discrete element method, employing the generalized Lagrange equation to accurately describe rock damage and failure processes[33,34]. The algorithm divides the model into block elements and interface elements. Each block element consists of one or more finite elements to characterize rock's continuous behavior. Interface elements include real interfaces (representing natural discontinuities such as natural fractures and weak planes) and virtual interfaces (providing potential propagation paths for hydraulic fracturing). Adjacent blocks are connected through normal and tangential springs that transmit interaction forces, where spring failure reflects rock fracture characteristics.

2.1 Solid constitutive model

Assuming the rock deformation follows linear elasticity and satisfies the small deformation hypothesis, the fracture propagation process is considered quasi-static[35]. All finite elements within the block elements satisfy stress equilibrium, and the matrix form of the stress field governing equation can be expressed as:

$$\boldsymbol{M}\ddot{\boldsymbol{u}}^e + \boldsymbol{C}\dot{\boldsymbol{u}}^e + \boldsymbol{K}\boldsymbol{u}^e = \boldsymbol{F}^e \tag{1}$$

where, $\ddot{\boldsymbol{u}}^e$, $\dot{\boldsymbol{u}}^e$, and $\boldsymbol{u}^e$ is the acceleration matrix, velocity matrix, and displacement matrix of all nodes in the element, respectively; $\boldsymbol{M}$, $\boldsymbol{C}$, $\boldsymbol{K}$, $\boldsymbol{F}^e$ is the element mass matrix, damping matrix, stiffness matrix, and external force respectively.

The CDEM employs an explicit Euler forward difference method for time-domain iterative solutions. The iterative formulation can be expressed as:

$$\begin{cases} \dot{\boldsymbol{u}}^{n+1} = \dot{\boldsymbol{u}}^n + \ddot{\boldsymbol{u}}^n \Delta t \\ \boldsymbol{u}^{n+1} = \boldsymbol{u}^n + \dot{\boldsymbol{u}}^{n+1} \Delta t \end{cases} \tag{2}$$

where, n is the iteration steps; Δt is the time step.

2.2 Failure criterion

Two adjacent block elements are connected via tangential and normal springs. The relative displacement at the contact point between neighboring blocks and the corresponding spring forces obey Hooke's law:

$$\Delta u_n = \frac{F_n}{K_n} = \frac{(\sigma_{n1} + \sigma_{n2})A}{2K_n} \tag{3}$$

$$\Delta u_t = \frac{F_t}{K_t} = \frac{(\sigma_{t1} + \sigma_{t2})A}{2K_t} \tag{4}$$

where, Δu_n, Δu_t are the normal displacement and tangential displacement; F_n, F_t are the normal force and tangential force; K_n, K_t are the normal stiffness and tangential stiffness of the spring; A is the contact area; σ_{n1}, σ_{n2} are the normal stress at the contact point; σ_{t1}, σ_{t2} are tangential stress at the contact point.

The Coulomb-Mohr criterion and maximum tensile stress criterion are adopted as the rock failure criteria to characterize tensile and shear failure modes. Specifically, the maximum tensile stress criterion can be expressed as:

$$\sigma_n \geq T \tag{5}$$

where, σ_n is the normal stress; T is the tensile strength;

The Coulomb-Mohr criterion can be expressed as:

$$\sigma_t > c + \sigma_n \tan\varphi \tag{6}$$

where, σ_t is the tangential stress; c, φ are the cohesion and internal friction angle, respectively.

2.3 Seepage calculation

Assuming the material is isotropic, the finite volume method is employed to separately compute the pore seepage field and fracture seepage field. Both fields satisfy Darcy's law and mass conservation[36]. When the nodal saturation reaches unity, the pore fluid pressure and fracture fluid pressure can be calculated according to Equations (7-8).

$$p_p^F = -\sum_{t=0}^{t} \left(K^F \frac{(Q^F + Q_{app})}{nV} \Delta t\right) \tag{7}$$

$$p_p^F = -\sum_{t=0}^{t} \left(K^F \frac{(Q^F + Q_{app})}{nV} \Delta t\right) \tag{8}$$

where, p_p^E is the pore fluid pressure, p_p^F is the fracture fluid pressure, k^E is the permeability coefficient of the porous matrix , k^F is the fracture permeability coefficient, Q^E is the pore nodal flow rate , Q^F is the fracture nodal flow rate , Q_{app} is the external flow boundary condition.

The total pressure at pore element nodes and fracture element nodes can be determined according to Eq. (9~10).

$$P^E = p_p^E - s^E r(xg_x + yg_y + zg_z), \tag{9}$$

$$P^F = p_p^F - s^F r(xg_x + yg_y + zg_z), \tag{10}$$

where, P^E is the total pressure at pore element nodes, P^F is the total pressure at fracture element nodes, s^E is the average saturation of pore elements, s^F is the average saturation of fracture elements, g_x, g_x, g_x are the global components of gravitational acceleration, r is the fluid density.

3 Model construct and parameters

3.1 The model construction of single hydraulic fracture and single natural fracture

Fig.1 shows the schematic diagram of the single hydraulic fracture and single natural fracture model. The model dimensions are 10 m × 10 m × 2 m. The natural fracture is predefined as a hard line, with its center located 5 m from the injection point, measuring 2 m × 2 m in size. The model was discretized using the open-source software Gmsh[37] (Version [2.16.0]; https://gmsh.info/), comprising a total of 960 block elements and 1,240 interface elements. The mesh size is set at 1 m. The block elements employ triangular prism meshes, while the interface elements utilize quadrilateral meshes. The model is primarily used to investigate the interaction mechanisms between hydraulic fractures and natural fractures, comparing the results with theoretical criteria to validate the reliability of the proposed interaction model. The study systematically examines hydraulic-natural fracture interactions under varying natural fracture angles (30°, 45°, 60°, and 90°) and different horizontal stress differences (2 MPa, 6 MPa, 10 MPa, and 14 MPa). Model parameters are provided in Table 1, and detailed simulation schemes are listed in Table 2.

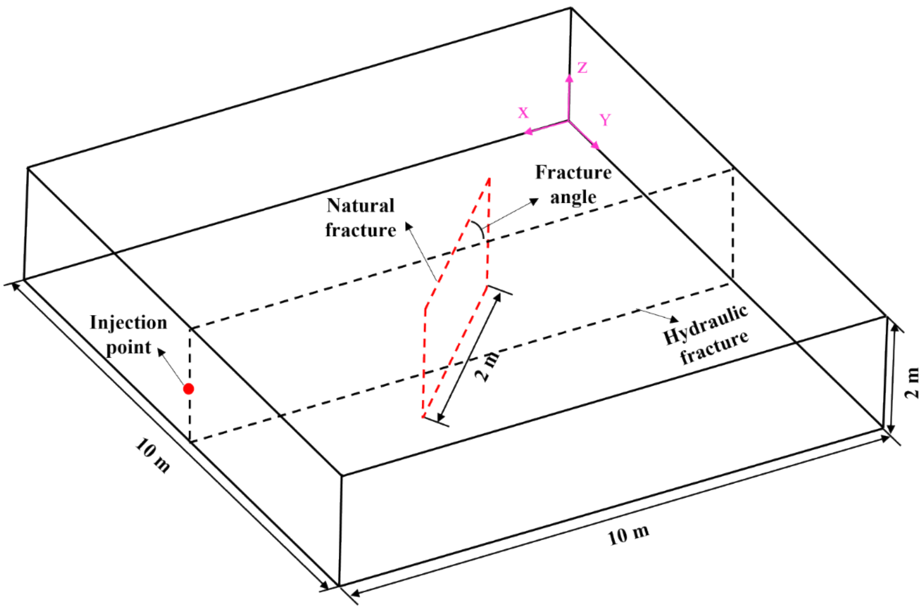

Fig. 1 The schematic diagram of single hydraulic fracture and natural fracture model

Table 1 The model parameter

Types	Parameter	Value	Unit
Rock Matrix	In-situ stress (X/Y/Z)	34/20/35	MPa
	Elastic modulus	50	GPa
	Poisson's Ratio	0.22	/
	Tensile Strength	3	MPa
	Cohesion	8	MPa
	Internal Friction Angle	40	°
	Loss Coefficient	1e-14	m^2/Pa/s
Natural fracture	Tensile Strength	0	MPa
	Cohesion	1	MPa
	Internal Friction Angle	20	°
Injection parameter	Injection rate	0.001	m^3/s
	Fluid viscosity	1	mPa•s

Table 2 The parameter simulation scheme

No.	Stress	Natural fracture	Tensile strength/ Cohesion/	Injection	Viscosity

	difference （MPa）	angle （°）	Internal friction angle （MPa/MPa/°）	rate （m^3/s）	（mPa•s）
1	0	30	0/1/20	0.001	1
2	5	30			
3	10	30			
4	15	30			
5	0	45			
6	5	45			
7	10	45			
8	15	45			
9	0	60			
10	5	60			
11	10	60			
12	15	60			
13	0	90			
14	5	90			
15	10	90			
16	15	90			

3.2 The model construction of single hydraulic fracture and the natural fracture network

Fig. 2 shows the schematic of a single hydraulic fracture interacting with the natural fracture network. The model sizes is 30 m × 30 m × 2 m, with the injection well centered at (15 m, 15 m, 1 m). The naturally fractured system contains uniformly distributed discrete fractures, each measuring 2 m × 2 m × 2 m with 2 m spacing between adjacent fractures. The computational mesh was generated using Gmsh software with the element size of 1 m. The matrix was discretized using triangular prism elements, while the interface network was represented by quadrilateral elements.

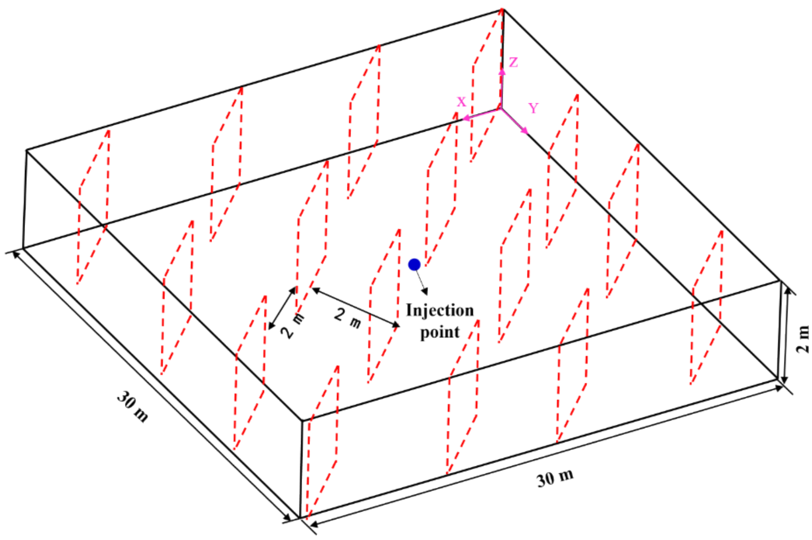

Fig. 2 The schematic diagram of single hydraulic fracture and natural fractures model

The model investigates hydraulic fracture propagation in naturally fractured reservoirs, analyzing geological parameters (stress difference, natural fracture orientation and intensity) and engineering parameters (injection rate and fluid viscosity) on fracture propagation. Model parameters are shown in Table 1, with simulation schemes detailed in Table 3. Cases 1-16 investigate the effect of different stress differences (0, 5, 10, 15 MPa) and natural fracture orientations (0°, 30°, 60°, 90°) on fracture propagation. Cases 17-19 investigate the effect of natural fracture intensity at 0 MPa stress anisotropy with dual natural fracture sets (60° and 120°) on fracture propagation. Cases 17, 20, and 21 analyze injection rate impacts under the stress difference of 0 MPa and dual natural fracture sets of 60° and 120°.

Table 3 The parameter simulation scheme

No.	Stress difference (MPa)	Natural fracture angle (°)	Tensile strength/ Cohesion/ Internal friction angle (MPa/MPa/°)	Injection rate (m^3/s)	Viscosity (mPa•s)
1	0	30			
2	0	45	0/1/20	0.005	10
3	0	60			

4	0	90			
5	5	30			
6	5	45			
7	5	60			
8	5	90			
9	10	30			
10	10	45			
11	10	60			
12	10	90			
13	15	30			
14	15	45			
15	15	60			
16	15	90			
17	0	60+120	0/1/20	0.005	10
18	0	60+120	1.5/4/20	0.005	10
19	0	60+120	0/0/0		
20	0	60+120	0/1/20	0.001	10
21	0	60+120	0/1/20	0.01	10

4 The results of interactions between hydraulic fracture and single natural fracture

Fig. 3 shows the interaction patterns between hydraulic fracture and natural fracture under different stress differences and natural fracture angles. The results show that the interaction modes can be categorized into three types: (1) fully activating the natural fracture; (2) partially activating the natural fracture; (3) crossing the natural fracture. When the natural fracture angle is 30° or 45°, the natural fractures are activated under all stress differences. For natural fracture angles exceeding 60°, the hydraulic fractures cross the natural fractures when the stress difference exceeds 2 MPa.

Fig. 3 shows the interaction patterns between the hydraulic fracture (HF) and natural fracture (NF) under different stress differences and NF orientations. Three interaction modes are observed: (1) full activation of the NF; (2) partial activation of the NF; and (3) HF crossing. When the NF angle is 30° or 45°, the NFs are activated under all stress differences. This is because low-angle NFs are subjected to a lower normal stress and a higher shear component of the far-field stress, which promotes shear slip and tensile dilation. As a result, the energy required for HF diversion along the NF plane is lower than that needed for direct propagation, making NF activation more favorable. In contrast, NFs with orientations greater than 60° experience significantly higher normal stress, which suppresses both shear displacement and tensile opening. When the horizontal stress difference exceeds 2 MPa, the driving stress intensity at the HF tip becomes sufficiently large to overcome the sliding potential of the high-angle NF. Under these conditions, the HF maintains its trajectory and crosses the NF rather than being arrested or diverted. Furthermore, increased confining stress strengthens the NF by increasing normal stress on the fracture plane, which further inhibits NF activation and promotes HF crossing. These mechanisms explain the observed transition from NF activation to HF crossing with increasing fracture angle and stress difference.

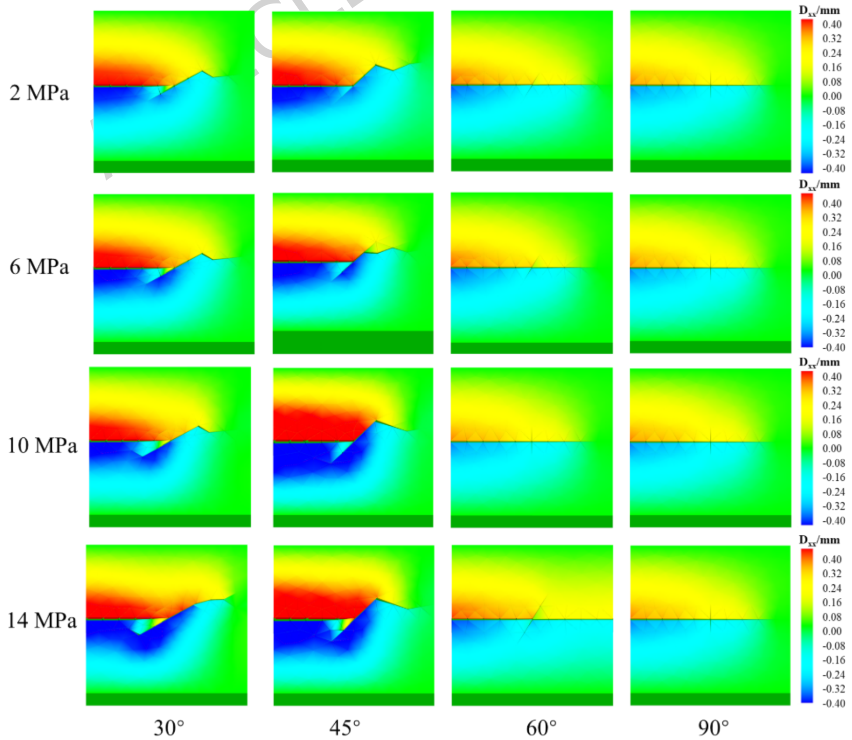

Fig. 3 The interaction pattern of hydraulic fracture and natural fracture under different stress

difference and natural fracture angle

Fig. 4 compares the simulation results of this study with Blanton's criterion. The area above the curve indicates hydraulic fracture penetration through natural fractures, while the region below the curve signifies natural fracture activation by hydraulic fracturing. The results demonstrate good agreement with Blanton's criterion. Specifically, hydraulic fractures tend to activate natural fractures even under high stress difference when the natural fracture angle is less than 45°. Conversely, when natural fractures are oriented at angles exceeding 60°, hydraulic fractures will penetrate through them even at low stress difference.

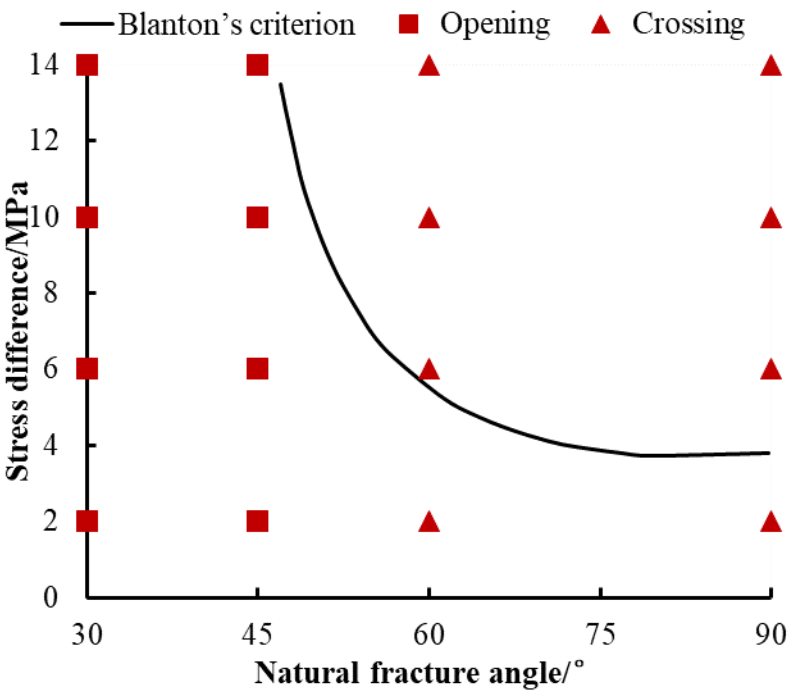

Fig. 4 Comparison of numerical simulation and Blanton's criterion

5 The results of interactions between hydraulic fracture and natural fracture network

5.1 The effect of natural fracture angle and stress difference

(1) The natural fracture network with 30°

Fig. 5 shows the interaction patterns between hydraulic fractures and a 30° natural fracture network under different stress differences. It can be observed that at 0 MPa stress difference, the hydraulic fracture activates the natural fractures and propagates along their orientation. Under a 5 MPa stress difference, the hydraulic fracture initially extends in the direction of the maximum horizontal principal stress, then activates and diverts along the natural fractures upon encountering them. When the stress difference exceeds 10 MPa, the natural fractures are no longer activated, and the hydraulic fracture propagates solely along the direction of the maximum horizontal principal stress.

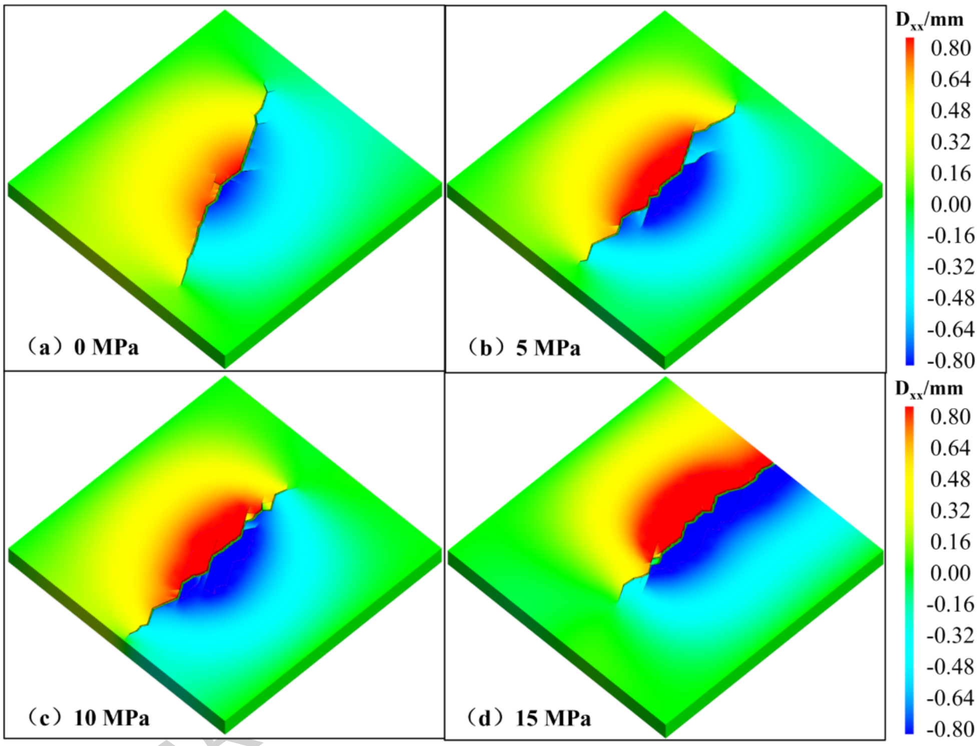

Fig. 5 The hydraulic fracture morphology under different stress difference

Fig. 6(a) shows the injection pressure evolution curves versus time under different stress differences. The results indicate that within the 30° natural fracture network, the maximum breakdown pressure of 29.6 MPa occurs at 0 MPa stress difference. For stress differences exceeding 5 MPa, the breakdown pressures remain relatively consistent. Additionally, the fracture propagation pressure shows a gradual increase with rising stress difference. Fig. 6(b) shows the evolution of fracture degree with time under various stress differences. At 20 s, the highest breakdown degree occurs at 15 MPa, followed by 0 MPa and 10 MPa, while 5 MPa exhibits the lowest value. This phenomenon primarily results from the 15 MPa hydraulic fracture propagating along the maximum horizontal principal stress direction, enabling earlier arrival at the model boundary. Under the constant-pressure boundary condition employed in this study, the hydraulic fracture stop propagation upon reaching the boundary and undergoes pressure accumulation followed by re-initiation. Fig. 6(b) clearly demonstrates a significant increase in fracture breakdown degree at 16 s, attributable to this pressure buildup and subsequent re-fracturing process.

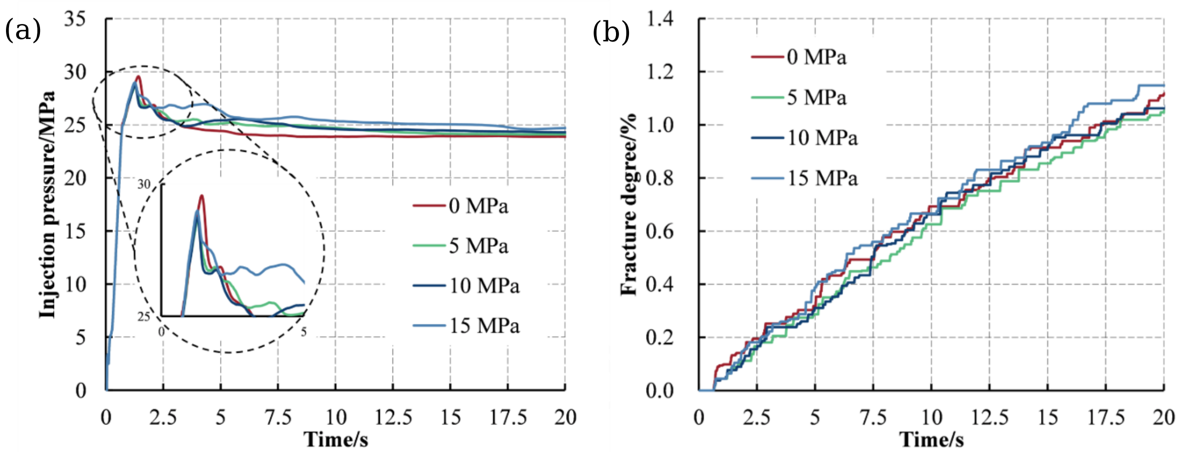

Fig. 6 The injection pressure (a) and fracture degree (b) with the time evolution

(2) The natural fracture network with 45°

Fig. 7 shows the interaction patterns between hydraulic fractures and 45° natural fracture networks under different stress differences. The results show that at 0 MPa stress difference, three distinct fracture branches develop: one propagating along the maximum horizontal principal stress direction, one extending along the natural fracture orientation, and one advancing perpendicular to the natural fractures. However, when the stress difference exceeds 5 MPa, the hydraulic fractures predominantly propagate along the maximum horizontal principal stress direction.

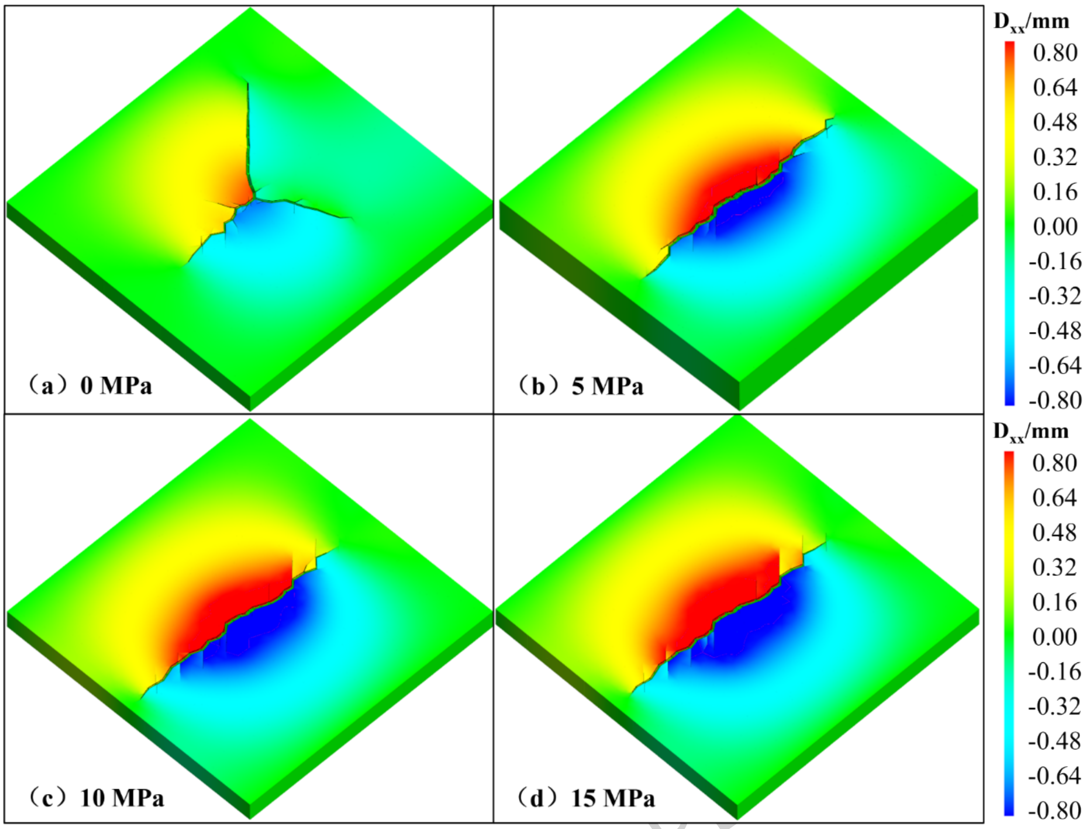

Fig. 7 The hydraulic fracture morphology under different stress difference

Fig. 8 (a) shows the injection pressure evolution curves under different stress differences. The results show that at 0 MPa, two distinct breakdown pressures are observed due to the formation of branch fractures. The breakdown pressure gradually increases with increasing stress difference, reaching a maximum value of 29.6 MPa at 15 MPa. Fig. 8 (b) shows the fracture degree evolution curves under various stress differences. At 20 s, the fracture degree follows the order: 0 MPa > 15 MPa > 10 MPa > 5 MPa. This demonstrates that during hydraulic fracturing, simply activating natural fractures does not enhance the stimulated reservoir volume. Conversely, the formation of branch fractures while activating natural fractures during hydraulic fracture propagation can significantly improve the stimulation area.

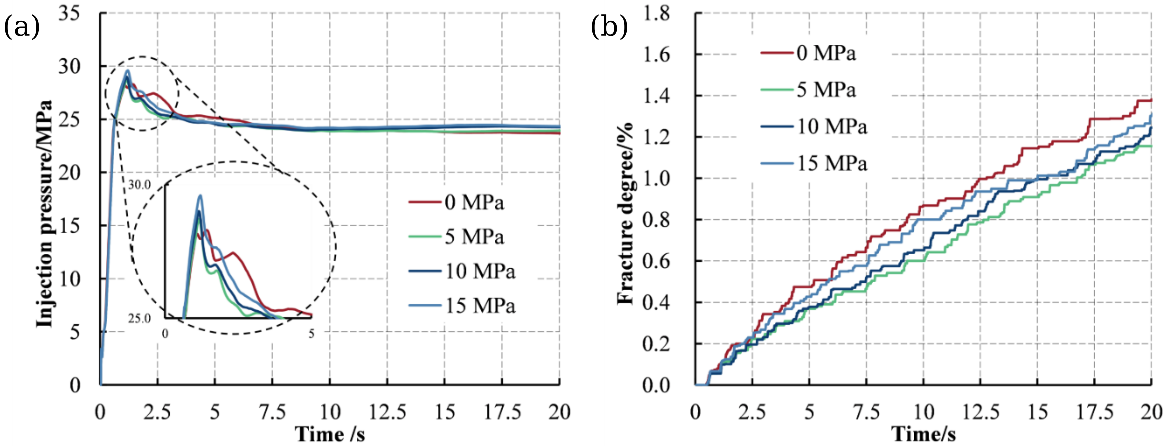

Fig. 8 The injection pressure (a) and fracture degree (b) with the time evolution

(3) The natural fracture network with 60°

Fig. 9 shows the interaction patterns between hydraulic fractures and 60° natural fracture networks under different stress differences. At 0 MPa stress difference, three branch fractures form near the injection point, with one propagating along the 60° natural fracture direction and two extending perpendicular to natural fractures at higher propagation velocities. When the stress difference exceeds 5 MPa, natural fractures are nearly completely deactivated and hydraulic fractures propagate predominantly along the maximum horizontal principal stress direction. The results clearly demonstrate a critical stress threshold (5 MPa) that governs the transition from complex fracture network development to simplified stress-dominated propagation for 60° natural fracture systems.

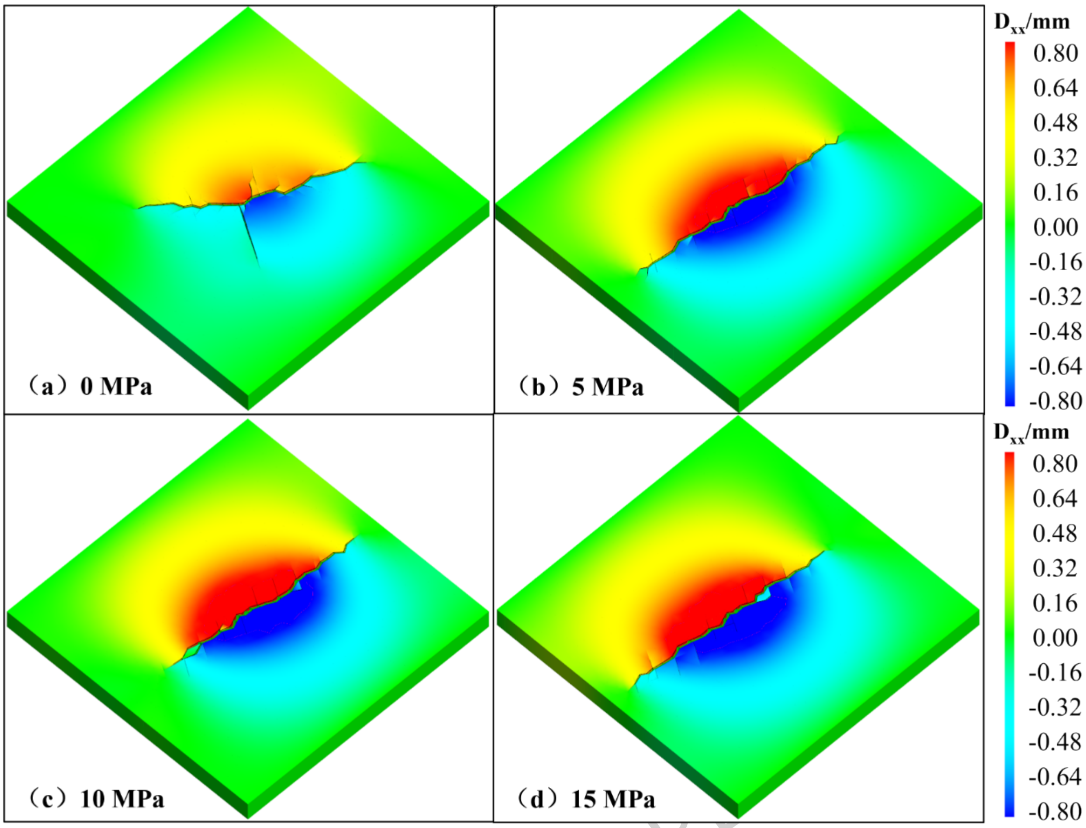

Fig. 9 The hydraulic fracture morphology under different stress difference

Fig. 10(a) shows the evolution of injection pressure with time under different stress differences. The results show that the maximum breakdown pressure of 29.3 MPa occurs at 0 MPa stress difference, while the breakdown pressure gradually increases as the stress difference rises from 5 MPa to 15 MPa. Fig. 10(b) presents the evolution of fracture breakdown degree with time under various stress differences, revealing that the highest breakdown degree occurs at 15 MPa, followed by 10 MPa, with 0 MPa and 5 MPa showing comparable values. This behavior primarily results from distinct fracture propagation mechanisms: under high stress differences, fractures propagate predominantly along the maximum horizontal principal stress direction with relatively larger fracture widths, while under low stress differences, hydraulic fracture propagation is less constrained by stress differences and is influenced by the activation of partial branch fractures in natural fractures, leading to relatively smaller fracture widths. Consequently, when the activated length of natural fractures is relatively small, the overall stimulated area is less effective compared to the single dominant fracture formed under high stress difference conditions.

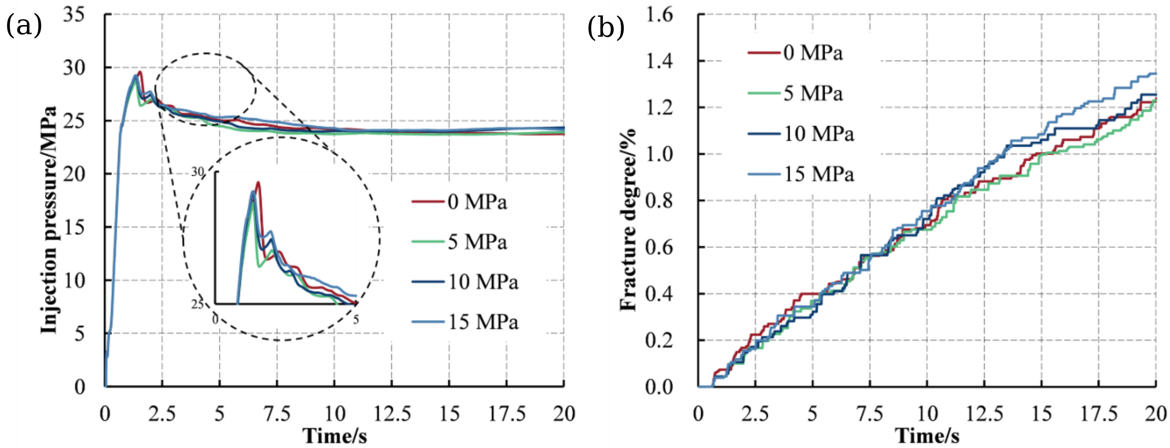

Fig. 10 The injection pressure (a) and fracture degree (b) with the time evolution

(4) The natural fracture network with 90°

Fig. 11 shows the interaction patterns between hydraulic fractures and 90° natural fracture networks under varying stress differences. The results demonstrate that at 0 MPa stress difference, three branch fractures form near the injection point: one propagating along the 90° natural fracture orientation while the other two extend horizontally. When the stress difference exceeds 5 MPa, natural fractures remain completely inactive and hydraulic fractures propagate exclusively along the maximum horizontal principal stress direction. This behavior confirms the critical 5 MPa stress threshold observed in other configurations, beyond which fracture propagation becomes purely stress-dominated regardless of natural fracture orientation. The consistent 5 MPa transition threshold across different natural fracture angles (30°, 45°, 60°, and 90°) suggests a universal stress-controlled mechanism governing the interaction between hydraulic and natural fractures in this system.

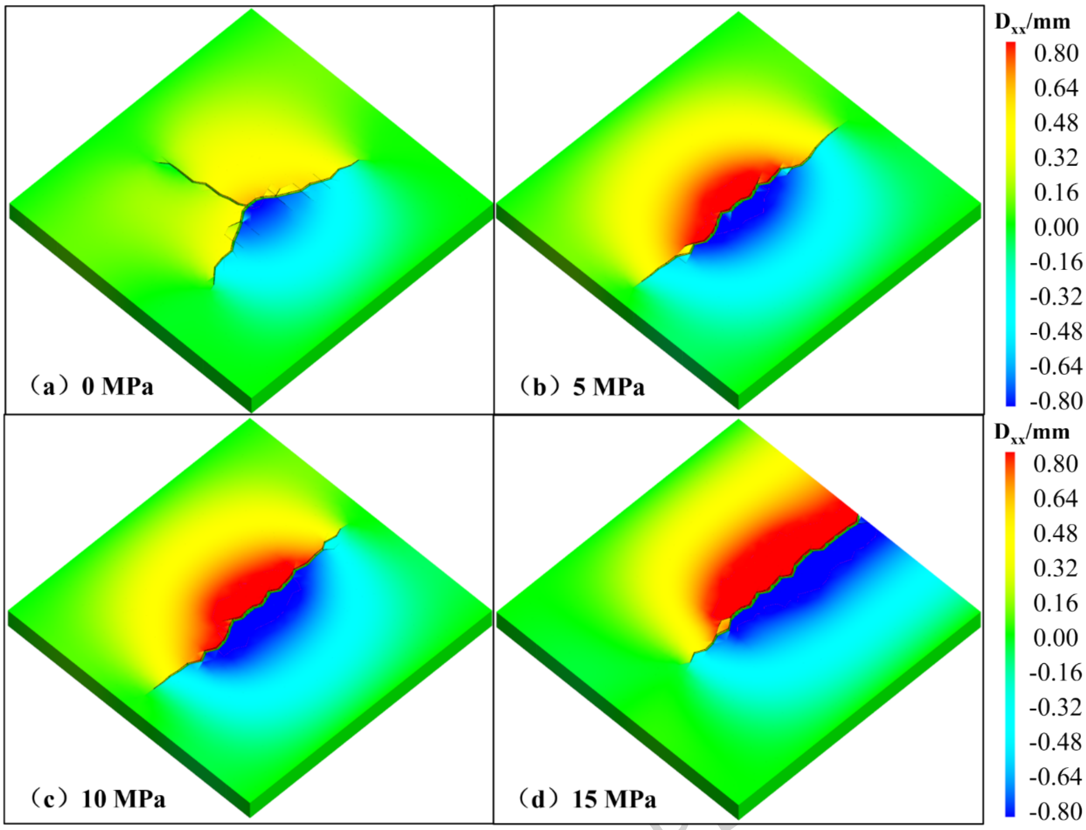

Fig. 11 The hydraulic fracture morphology under different stress difference

Fig. 12 (a) shows the evolution pattern of injection pressure under different stress differences, showing that the maximum breakdown pressure of 28.7 MPa occurs at 0 MPa. While the breakdown pressure shows insignificant variation as the stress difference increases from 5 MPa to 15 MPa, the fracture propagation pressure exhibits a substantial increase at 15 MPa. Fig. 12 (b) displays the evolution of fracture breakdown degree with time under various stress differences, revealing that the 0 MPa condition achieves significantly higher breakdown degree due to the formation of branch fractures and activation of numerous 90° natural fractures. In contrast, the breakdown degree remains relatively consistent across 5-15 MPa stress differences as the fractures propagate predominantly along the maximum horizontal principal stress direction in these cases. The results demonstrate that complex fracture networks with multiple branches (0 MPa) provide superior stimulation effectiveness compared to single planar fractures (5-15 MPa), despite requiring higher initial breakdown pressures.

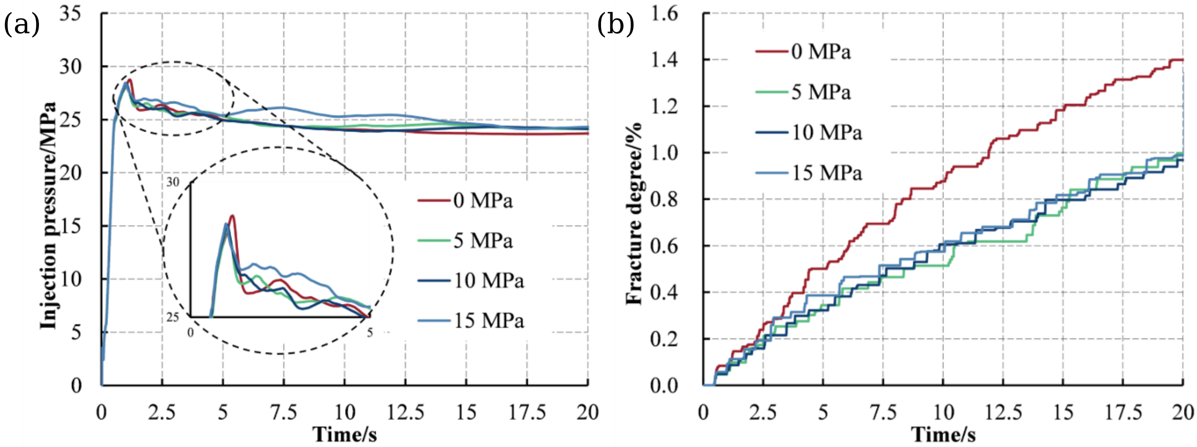

Fig. 12 The injection pressure (a) and fracture degree (b) with the time evolution

5.2 The effect of natural fracture strength

To investigate the influence of natural fracture strength on hydraulic fracture propagation, this study established three types of natural fracture networks with different cementation strengths by varying their tensile strength, cohesion, and internal friction angle. The natural fracture networks consisted of conjugate fractures at 60° and 120°, categorized as: (a) uncemented (zero tensile strength, cohesion, and internal friction angle); (b) weakly cemented (0 MPa tensile strength, 1 MPa cohesion, and 20° internal friction angle); and (c) strongly cemented (1.5 MPa tensile strength, 4 MPa cohesion, and 20° internal friction angle). Fig. 13 shows the interaction patterns between hydraulic fractures and natural fractures under different cementation strengths. The results show that at 0 MPa in-situ stress difference, the number of branch fractures increases with natural fracture strength. This occurs because, under uncemented conditions, hydraulic fractures tend to propagate along low-angle natural fractures following the principle of energy minimization. However, as natural fracture strength increases, fracture opening becomes more difficult. Consequently, in the absence of significant stress differences, hydraulic fractures tend to develop multiple branch fractures rather than following a single dominant path.

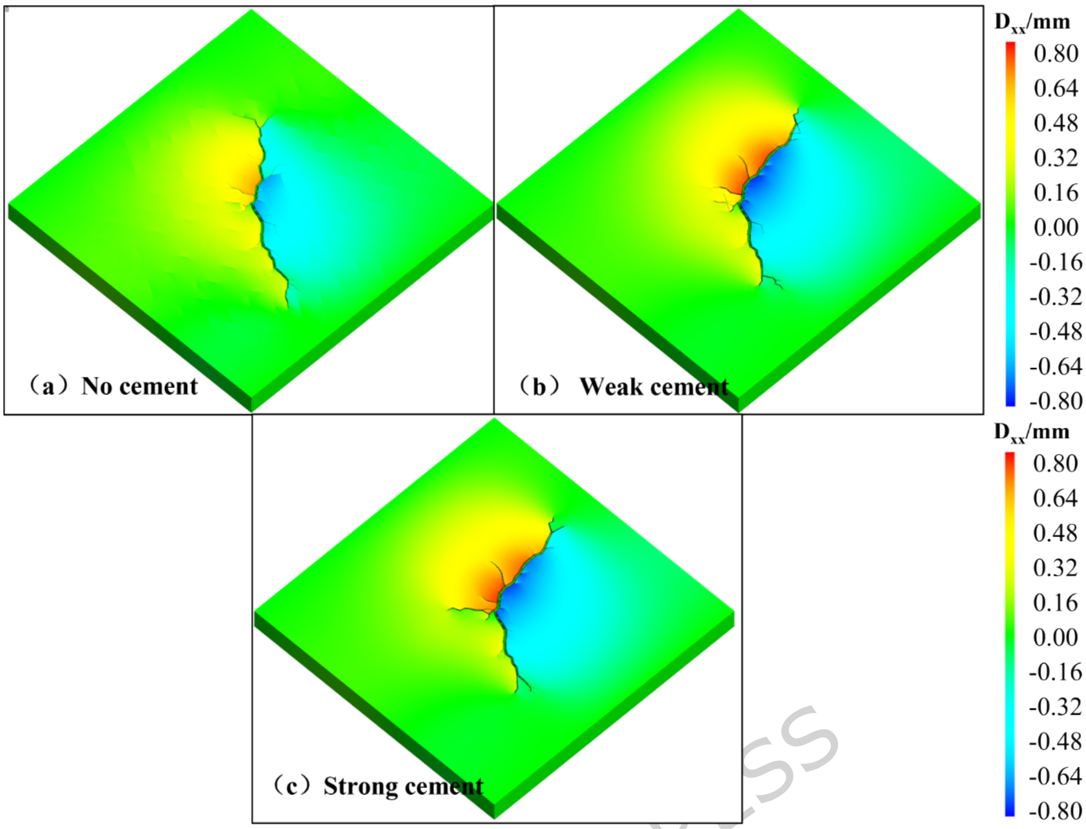

Fig. 13 The hydraulic fracture morphology under different cementation strength

Fig. 14(a) shows the evolution of injection pressure with time under different natural fracture strengths. The result show that the breakdown pressure gradually increases with higher cementation strength. Fig. 14(b) displays the evolution of fracture degree with time for various natural fracture strengths, revealing that the weakly cemented condition achieves the maximum breakdown degree, while both uncemented and strongly cemented cases exhibit relatively lower values. Under weakly cemented conditions, the fracture interface has moderate cohesion and stiffness, so hydraulic pressure can partially debond and open the interface, inducing both shear slip and tensile dilation along the natural fracture. At the same time, the remaining bond strength is sufficient to transfer stress perturbations into the surrounding matrix, which promotes repeated branching and re-initiation of fractures at the natural-fracture tips. This leads to the highest fracture complexity and stimulated volume. In contrast, strongly cemented natural fractures behave similarly to intact rock; the high cohesion and normal stiffness favor direct crossing of the interface and suppress fracture diversion, resulting in a simpler, more planar hydraulic-fracture geometry. Under uncemented conditions, the interfaces are easily activated and quickly become dominant, highly conductive flow channels. Fluid then preferentially migrates along these pre-existing open fractures, reducing the net pressure at the hydraulic-fracture tip and limiting the formation of new branches in the matrix. Therefore, both very low and very high interface strengths tend to reduce the degree of newly generated fracturing, whereas intermediate (weakly cemented) conditions promote the most complex fracture network.

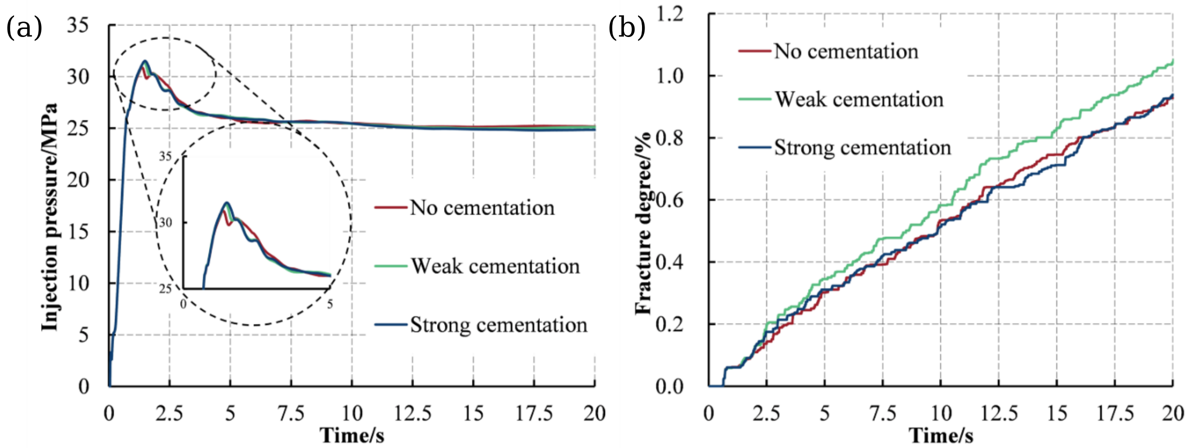

Fig. 14 The injection pressure (a) and fracture degree (b) with the time evolution

5.3 The effect of injection rate

To investigate the influence of injection rate on hydraulic fracture propagation, this study simulated three different injection rate conditions: (a) 0.001 m³/s, (b) 0.005 m³/s, and (c) 0.01 m³/s, with corresponding simulation times of 100 s, 20 s, and 10 s respectively to maintain consistent total injection volume. Fig. 15 presents the hydraulic fracture propagation patterns under different injection rates. Under low injection rate (0.001 m³/s), natural fractures were rarely activated, resulting in three branch fractures - two propagating horizontally and one extending perpendicular to the horizontal direction. At the medium injection rate (0.005 m³/s), limited natural fracture activation occurred, forming two branch fractures: one propagating horizontally and another following the natural fracture orientation. The high injection rate condition (0.01 m³/s) demonstrated significantly improved natural fracture activation due to rapid pressure buildup, ultimately developing three branch fractures - one propagating along natural fractures while continuously activating them, and the other two crossing through natural fractures during extension.

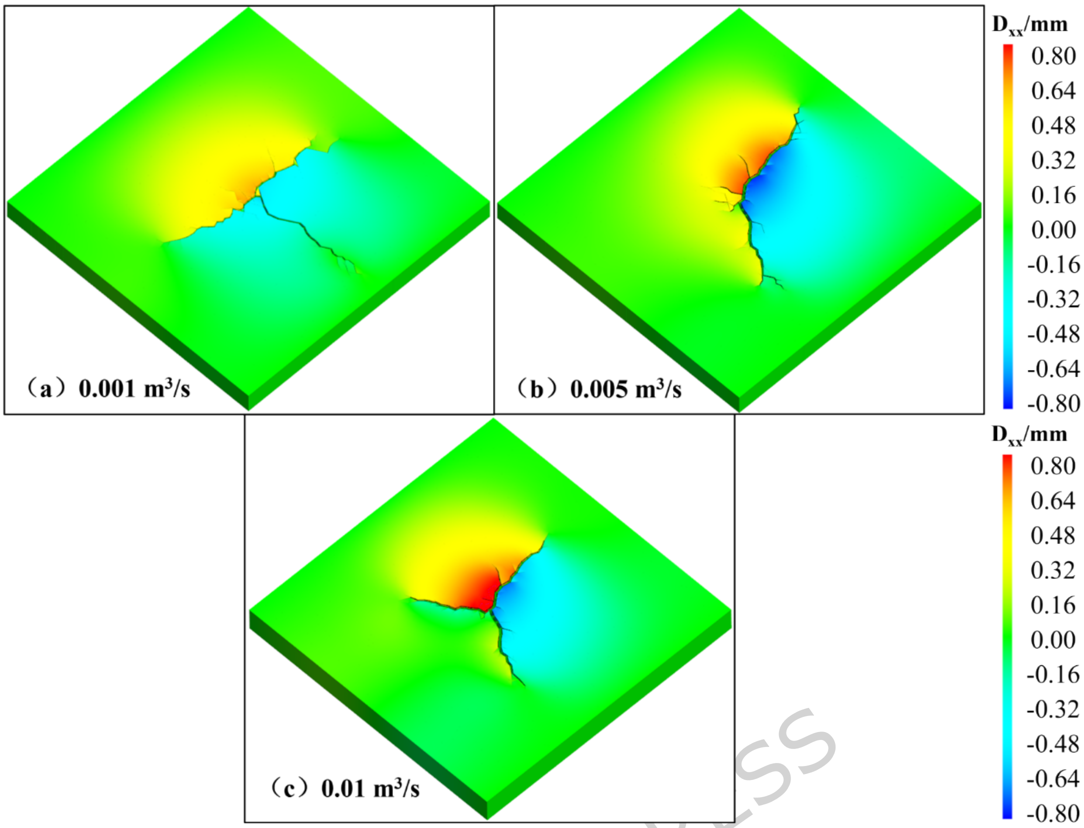

Fig. 15 The hydraulic fracture morphology under different flow rate

Fig. 16(a) presents the evolution of injection pressure with time under different injection rates. The results demonstrate a significant increase in rock breakdown pressure with higher injection rates. At 0.001 m^3/s, two distinct breakdown pressure peaks occur (26.1 MPa and 26.4 MPa). When the rate increases to 0.005 m^3/s, the breakdown pressure rises to 31.3 MPa, and further increases to 34.3 MPa at 0.01 m^3/s. Fig. 16(b) shows the fracture breakdown degree evolution under various injection rates. While the rate of breakdown degree increase accelerates with higher injection rates, the final breakdown degree at equal injected volume reveals an inverse relationship: the 0.001 m^3/s condition achieves the maximum breakdown degree, whereas 0.01 m^3/s yields the minimum value. Under a high injection rate, the rapid increase in fluid pressure generates a stronger driving force at the fracture tip. This promotes rapid dilation of the main hydraulic fracture near the wellbore and facilitates hydraulic fracture crossing rather than the reactivation of natural fractures. As a result, fewer shear-activated natural fractures and fewer secondary branches are formed, which reduces the overall fracture complexity. In contrast, under a low injection rate and with the same total injected volume, pressure buildup is slower, allowing more time for stress redistribution around the fracture tip. This condition favors the shear activation of natural fractures, leading to the formation of multiple secondary and branching fractures as well as a more tortuous propagation path. Consequently, fracture complexity is significantly higher at lower injection rates.

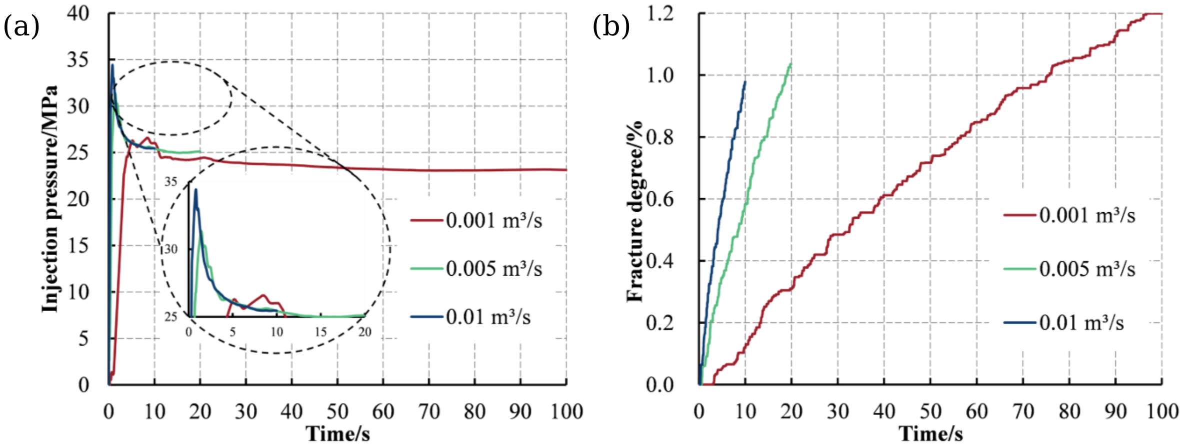

Fig. 16 The injection pressure (a) and fracture degree (b) with the time evolution

6 Conclusion

In this study, a stress–seepage–fracture multi-field coupling algorithm based on a continuous–discontinuous framework was developed to investigate the interaction between hydraulic fractures and natural fractures in fractured reservoirs. The results clarify the mechanistic relationships among stress difference, natural fracture orientation, and the resulting hydraulic fracture–natural fracture interaction mode, thereby providing new theoretical insights and predictive capability for fracture propagation behavior.

(1) Single natural fracture: The simulations show that natural fractures with orientations of 30° and 45° are consistently activated under all tested stress differences due to favorable shear stress conditions. When the natural fracture angle exceeds 60°, hydraulic fractures tend to cross the natural fracture once the horizontal stress difference is greater than 2 MPa. This identifies a critical threshold for the transition from fracture activation to fracture crossing.

(2) Natural fracture networks: For networks with multiple fracture orientations, the stress difference exerts a dominant influence on the overall fracture geometry. When the

stress difference exceeds 5 MPa, hydraulic fractures predominantly propagate in the direction of the maximum horizontal principal stress, resulting in a more linear, directionally controlled fracture morphology.

(3) Effect of natural-fracture mechanical properties: The number of branching fractures increases as the natural fracture strength increases. Under uncemented conditions, hydraulic fractures preferentially propagate along low-angle natural fractures due to energy-minimization mechanisms.

7 Limitations and Outlook

Despite these advances, the present model still adopts several simplifying assumptions. The simulations are based on quasi-static deformation and single-phase flow, without incorporating proppant transport, fracture roughness, or fluid leak-off heterogeneity. In addition, although the model is three-dimensional in mesh structure, fracture behavior is effectively constrained to quasi-2D propagation due to computational cost considerations. These simplifications may limit the direct applicability of the results to highly heterogeneous or strongly three-dimensional reservoirs. Future work will focus on incorporating multi-phase flow, proppant transport mechanisms, and fully three-dimensional fracture propagation to better capture the complexity of actual field operations. These developments are expected to support more reliable prediction of fracture network geometry and more effective optimization of hydraulic fracturing strategies in naturally fractured reservoirs.

Funding

Supported by the National Natural Science Foundation of China (No. 52174045, No. U23B2084 and No.5241002).

Data availability

The data that support the findings of this study are available from the corresponding authors upon reasonable request.

References

[1] J. Yu, N. Li, B. Hui, W. Zhao, Y. Li, J. Kang, P. Hu, and Y. Chen, "Experimental simulation of fracture propagation and extension in hydraulic fracturing: A state-of-the-art review," Fuel **363**, 131021 (2024).

[2] P. Yang, S. Zhang, Y. Zou, A. Zhong, F. Yang, D. Zhu, and M. Chen, "Numerical Simulation of integrated three-dimensional hydraulic fracture propagation and proppant transport in multi-well pad fracturing," Computers and Geotechnics **167**, 106075 (2024).

[3] G. Huang, M. Li, J. Chu, F. Zhou, and G. Lu, "Longitudinal propagation mechanisms of multiple fractures in heterogeneous multi-lithology stacked reservoirs: A continuum-discontinuum simulation study," Engineering Fracture Mechanics **322**, 111181 (2025).

[4] Y. Guo, L. Huang, and X. Li, "Experimental and numerical investigation on the fracture behavior of deep anisotropic shale reservoir under in-situ temperature," Energy **282**, 128969 (2023).

[5] Y. Xia, M. Yao, T. Li, H. Yang, and C. Tang, "Numerical analysis of hydraulic fracture propagation in deep shale reservoir with different injection strategies," Journal of Rock Mechanics and Geotechnical Engineering **16**(9), 3558–3574 (2024).

[6] L. Barale, S. Botta, F. Piana, S. Tallone, C. Fidelibus, C. Avataneo, F. Turci, R. Compagnoni, R. Cossio, and W. Alberto, "Estimation of natural asbestos content in rocks by fracture network modeling and petrographic characterization," Engineering Geology **271**, 105566 (2020).

[7] Z. Jinzhou, Q. Wang, H. Yongquan, Z. Chaoneng, and Z. Jin, "Prediction of Pore Pressure–Induced Stress Changes during Hydraulic Fracturing of Heterogeneous Reservoirs through Coupled Fluid Flow/Geomechanics," Journal of Engineering Mechanics **145**(12), 05019001 (2019).

[8] X. Weng, "Modeling of complex hydraulic fractures in naturally fractured formation," Journal of Unconventional Oil and Gas Resources **9**, 114–135 (2015).

[9] H. Zheng, C. Pu, and C. Sun, "Study on the interaction between hydraulic fracture and natural fracture based on extended finite element method," Engineering Fracture Mechanics **230**, 106981 (2020).

[10] E. Bakhshi, V. Rasouli, A. Ghorbani, M. Fatehi Marji, B. Damjanac, and X. Wan, "Lattice Numerical Simulations of Lab-Scale Hydraulic Fracture and Natural Interface Interaction," Rock Mech Rock Eng **52**(5), 1315–1337 (2019).

[11] D. Xiong, and X. Ma, "Influence of natural fractures on hydraulic fracture propagation behaviour," Engineering Fracture Mechanics **276**, 108932 (2022).

[12] A. Merzoug, V. Pandey, V. Rasouli, B. Damjanac, and H. Pu, "Comparison of lattice and pseudo 3D numerical simulation of tip screen out operation," Petroleum **9**(3), 454–467 (2023).

[13] J. Geertsma, and F. De Klerk, "A Rapid Method of Predicting Width and Extent of Hydraulically Induced Fractures," Journal of Petroleum Technology **21**(12), 1571–1581 (1969).

[14] T.K. Perkins, and L.R. Kern, "Widths of Hydraulic Fractures," Journal of Petroleum Technology **13**(09), 937–949 (1961).

[15] N. Zolfaghari, and A.P. Bunger, "Numerical model for a penny-shaped hydraulic fracture driven by laminar/turbulent fluid in an impermeable rock," International Journal of Solids and Structures **158**, 128–140 (2019).

[16] L.G. Barbosa, P.R. Cleto, M.A. Maedo, M. Camargo, E.A. Rodrigues, and O.L. Manzoli, "Simulation of the natural fractures influence on hydraulic fractures propagation using high aspect ratio interface elements," Computers and Geotechnics **179**, 107026 (2025).

[17] Y. Li, J. Deng, W. Liu, W. Yan, Y. Feng, W. Cao, P. Wang, and Y. Hou, "Numerical simulation of limited-entry multi-cluster fracturing in horizontal well," Journal of Petroleum Science and Engineering **152**, 443–455 (2017).

[18] M.-H. Li, F.-J. Zhou, B. Wang, X.-D. Hu, D.-B. Wang, X.-Y. Zhuang, S.-B. Han, and G.-P. Huang, "Numerical simulation on the multiple planar fracture propagation with perforation plugging in horizontal wells," Petroleum Science **19**(5), 2253–2267 (2022).

[19] B. Chen, S. Li, and D. Tang, "Numerical simulation study on hydraulic fracture propagation of multi-cluster fracturing of horizontal well in deep fractured coal seams," Engineering Fracture Mechanics **318**, 110983 (2025).

[20] S. Wang, L. Zhang, L. Cong, J. Zhou, D. Yang, X. Zhang, and Z. Han, "Three-Dimensional Lattice Modeling of Interaction Behavior Between Hydraulic Fractures and Natural Fractures with Varied Morphologies in Hot Dry Rock," Rock Mech Rock Eng **58**(3), 2971–2998 (2025).

[21] J. Zhou, L. Zhang, Z. Pan, and Z. Han, "Numerical studies of interactions between hydraulic and natural fractures by Smooth Joint Model," Journal of Natural Gas Science and Engineering **46**, 592–602 (2017).

[22] K. Wu, J. Olson, M.T. Balhoff, and W. Yu, "Numerical Analysis for Promoting Uniform Development of Simultaneous Multiple-Fracture Propagation in Horizontal Wells," SPE Production & Operations **32**(01), 41–50 (2017).

[23] W. Cheng, C. Lu, and B. Xiao, "Perforation Optimization of Intensive-Stage Fracturing in a Horizontal Well Using a Coupled 3D-DDM Fracture Model," Energies **14**(9), 2393 (2021).

[24] R. Gutierrez Escobar, E.C. Mejia Sanchez, D. Roehl, and C. Romanel, "Xfem modeling of stress shadowing in multiple hydraulic fractures in multi-layered formations," Journal of Natural Gas Science and Engineering **70**, 102950 (2019).

[25] D. Yang, Y. Zhou, X. Xia, S. Gu, Q. Xiong, and W. Chen, "Extended finite element modeling nonlinear hydro-mechanical process in saturated porous media containing crossing fractures," Computers and Geotechnics **111**, 209–221 (2019).

[26] Z. Chong, Q. Yao, X. Li, and J. Liu, "Investigations of seismicity induced by hydraulic fracturing in naturally fractured reservoirs based on moment tensors," Journal of Natural Gas Science and Engineering **81**, 103448 (2020).

[27] H. Fatahi, M.M. Hossain, and M. Sarmadivaleh, "Numerical and experimental investigation of the interaction of natural and propagated hydraulic fracture," Journal of Natural Gas Science and Engineering **37**, 409–424 (2017).

[28] S. Lyu, S. Wang, X. Chen, S. Wang, T. Wang, X. Shi, Q. Dong, and J. Li, "Natural fractures in soft coal seams and their effect on hydraulic fracture propagation: A field study," Journal of Petroleum Science and Engineering **192**, 107255 (2020).

[29] P. Zheng, Y. Xia, T. Yao, X. Jiang, P. Xiao, Z. He, and D. Zhou, "Formation mechanisms of hydraulic fracture network based on fracture interaction," Energy **243**, 123057 (2022).

[30] F. Shi, X. Wang, C. Liu, H. Liu, and H. Wu, "An XFEM-based method with reduction technique for modeling hydraulic fracture propagation in formations containing frictional natural fractures," Engineering Fracture Mechanics **173**, 64–90 (2017).

[31] J. Zhang, H. Yu, W. Xu, C. Lv, M. Micheal, F. Shi, and H. Wu, "A hybrid numerical approach for hydraulic fracturing in a naturally fractured formation combining the XFEM and phase-field model," Engineering Fracture Mechanics **271**, 108621 (2022).

[32] X. Zhu, C. Feng, P. Cheng, X. Wang, and S. Li, "A novel three-dimensional hydraulic fracturing model based on continuum–discontinuum element method," Computer Methods in Applied Mechanics and Engineering **383**, 113887 (2021).

[33] B. Zhang, T. Guo, M. Chen, J. Wang, J. Cao, H. Wang, and Z. Qu, "Effect of bedding planes and property contrast between layers on the propagation mechanism of hydraulic fracture height in shale reservoirs," Computers and Geotechnics **175**, 106715 (2024).

[34] X. Zhu, C. Feng, P. Cheng, X. Wang, and S. Li, "A novel three-dimensional hydraulic fracturing model based on continuum–discontinuum element method," Computer Methods in Applied Mechanics and Engineering **383**, 113887 (2021).

[35] Q. Ren, Y. Zhao, X. Zhu, Y. Zhou, Y. Jiang, P. Wang, and C. Zhang, "CDEM-based simulation of the 3D propagation of hydraulic fractures in heterogeneous Coalbed Methane reservoirs," Computers and Geotechnics **152**, 104992 (2022).

[36] G. Huang, X. Hu, F. Zhou, X. Li, E. Dong, and Z. Li, "A New Multi-Cluster Fracturing Simulation Model Coupled with Perforation Erosion: Based on the Continuous–Discontinuous Method," Rock Mech Rock Eng **56**(6), 3887–3901 (2023).

[37] C. Geuzaine, and J.-F. Remacle, "Gmsh: A 3-D finite element mesh generator with built-in pre- and post-processing facilities," International Journal for Numerical Methods in Engineering **79**(11), 1309–1331 (2009).